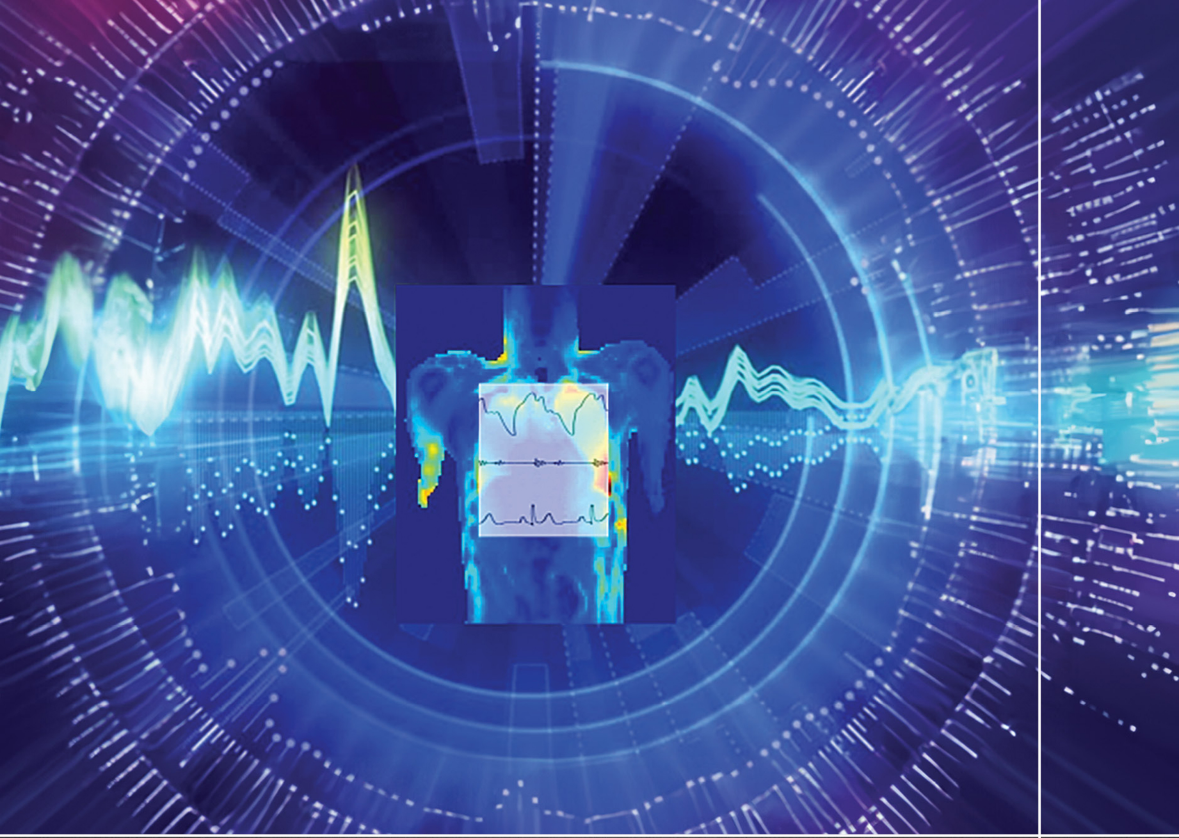

NONINVASIVE PHYSIOLOGICAL MEASUREMENT

WIRELESS MICROWAVE SENSING

James C. Lin

CRC Press
Taylor & Francis Group

Noninvasive Physiological Measurement

This book explains the principles and techniques of microwave physiological sensing and introduces fundamental results of the noninvasive sensing of physiological signatures, vital signs, as well as life detection. Specifically, noninvasive microwave techniques for contact, contactless, and remote sensing of circulatory and respiratory movements and physiological volume changes are discussed.

Noninvasive Physiological Measurement: Wireless Microwave Sensing, is written by a pioneering researcher in microwave noninvasive physiological sensing and leading global expert in microwaves in biology and medicine. The book reviews current advances in noninvasive cardiopulmonary sensing technology and measurement. It includes measurements of the vital signs and physiological signatures from laboratory research and clinical testing. The book discusses the applicable domains and scenarios in which there is an interaction of radio frequency (RF) and microwaves with biological matter in gas, fluid, or solid form, both from inside and outside of the human or animal body. The book also provides examples for healthcare monitoring and diagnostic applications through wearables, devices, or remote contactless sensors for physiological signals and signature, vital signs, and body motion sensing. This book is an essential guide to understanding the human body's interaction with microwaves and noninvasive physiological sensing and monitoring.

This book is intended for researchers and professionals in biomedical, electrical, and computer engineering with an interest in antenna, sensors, microwaves, signal processing, and medical applications. It will also be of interest to healthcare professionals, technologists, and practitioners interested in noninvasive physiological sensing and patient monitoring.

Dr. James C. Lin's pioneering work inspired many researchers to follow, and many more to follow them. He is recognized as one of the world's most renowned scientists who has studied microwave and RF radiation in biology and medicine. He has served as a professor of bioengineering, electrical and computer engineering, physiology and biophysics, and physical and rehabilitation medicine.

Noninvasive Physiological Measurement

Wireless Microwave Sensing

James C. Lin

CRC Press
Taylor & Francis Group
Boca Raton London New York

CRC Press is an imprint of the
Taylor & Francis Group, an **informa** business

Designed cover image: James C. Lin

First edition published 2024
by CRC Press
2385 NW Executive Center Drive, Suite 320, Boca Raton FL 33431

and by CRC Press
4 Park Square, Milton Park, Abingdon, Oxon, OX14 4RN

CRC Press is an imprint of Taylor & Francis Group, LLC

Library of Congress Cataloging-in-Publication Data

Names: Lin, James C., author.
Title: Noninvasive physiological measurement : wireless microwave sensing / James C. Lin.
Description: First edition. | Boca Raton, FL : CRC Press, 2024. | Includes bibliographical references and index.
Identifiers: LCCN 2023037654 (print) | LCCN 2023037655 (ebook) | ISBN 9781032319155 (hardback) | ISBN 9781032324753 (paperback) | ISBN 9781003315223 (ebook)
Subjects: MESH: Monitoring, Physiologic--methods | Microwaves | Wireless Technology
Classification: LCC RA569.3 (print) | LCC RA569.3 (ebook) | NLM WB 117 |
DDC 612/.014481--dc23/eng/20231113
LC record available at https://lccn.loc.gov/2023037654
LC ebook record available at https://lccn.loc.gov/2023037655

ISBN: 978-1-032-31915-5 (hbk)
ISBN: 978-1-032-32475-3 (pbk)
ISBN: 978-1-003-31522-3 (ebk)

DOI: 10.1201/9781003315223

Typeset in Times
by KnowledgeWorks Global Ltd.

To my grandsons:

Jonah Anderson, Lucas Theodore, and Kai Rong-Zhi

and

to the bright future that awaits each of them.

Taylor & Francis
Taylor & Francis Group
http://taylorandfrancis.com

Contents

List of Figures and Tables xiii
Preface xlv
Acknowledgments xlvii
About the Author xlix

Chapter 1 Introduction 1

1.1 Microwave and RF Radiation 3
1.1.1 Frequency Bands and Designations 4
1.2 Microwave Radar Technology 7
1.3 Physiological Sensing and Radiological Imaging 8
1.4 Microwave Sensing of Physiological Signatures and Movements 9
1.5 Optimal Microwave Frequency for Physiological Sensing 10
1.5.1 Remote, Near-Field, and Noncontact Strategy 11
1.5.2 Direct-Contact Strategy 12
1.6 Bench-Top Systems for Microwave Physiological Sensing 14
1.7 Telemedicine and the COVID-19 Pandemic 15
1.8 Protection Limits for Human Exposure to Microwaves 16
1.9 Organizing Principles of the Book 17

Chapter 2 Pioneering Investigations 21

2.1 A Scientific Research Journey 21
2.1.1 Respiratory Measurement and Microwave Cardiography 22
2.1.2 Vital-Sign Sensing 23
2.1.3 Arterial Pressure Pulse Wave and Cerebral Edema 24
2.1.4 Translational Research 25
2.1.5 DARPA Workshop on Noninvasive Blood Pressure Monitoring 29
2.1.6 DARPA RadioBio—A Sensing Challenge 30
2.1.7 A Side Bar—Microwave and Blood–Brain Barrier (BBB) Interactions: A Different Kind of Sensing 32
2.2 Microwave Sensing of Physiological Signatures and Volume Changes in the 1970s 34
2.2.1 Respiratory Activity Measurement 35
2.2.2 Measurement of Heart Rate and Sensing of Cardiac Events 39
2.2.3 Noninvasive Monitoring Fluid Buildup in the Lungs 41

2.3 Microwave Sensing of Vital Signs and Arterial Pulses in the 1980s 43
2.3.1 Remote Contactless Sensing of Vital Signs 43
2.3.2 Arterial Pulse Wave and Pressure Sensing 47
2.3.3 Cerebral Edemas and Extravasations 49
2.4 A Summary 50

Chapter 3 Microwave Propagation, Reflection, and Scattering 58

3.1 The Maxwell Equations 59
3.2 The Wave Equation 62
3.3 Boundary Conditions at Material Interfaces 63
3.4 Energy Storage and Power Flow 65
3.5 Plane Waves and Far-Zone Field 66
3.6 Polarization and Propagation of Plane Waves 67
3.6.1 Plane Waves in Free Space 69
3.6.2 Plane Waves in Lossy or Biological Media 69
3.7 Reflection and Transmission at Interfaces 71
3.8 Refraction of Microwave and RF Radiation 74
3.9 Radiation of Electromagnetic Energy 76
3.9.1 The Short Dipole Antenna 77
3.9.2 Near-Zone Radiation 78
3.9.3 Antenna Receiving Characteristics 82
3.9.4 Radar Cross Section 83
3.9.5 Conventional Antenna Configurations and Radiation Patterns 84
3.9.6 Microstrip Patch and Array Antennas 88

Chapter 4 Microwave Property of Living Matter 94

4.1 Frequency Dependence of Dielectric Permittivity 94
4.2 Dielectric Relaxation Processes 96
4.2.1 Low-Loss Dielectric Materials 97
4.2.2 Lossy Dielectrics at Low Frequencies 98
4.2.3 Biological Materials 100
4.3 Temperature Dependence of Dielectric Properties 101
4.3.1 Temperature Dependence of Measured Tissue Dielectric Permittivity 102
4.4 Measured and Modeled Tissue Permittivity Data 104
4.4.1 Permittivity of Water 105
4.4.2 Measured Tissue Permittivity 107
4.4.3 Debye Modeling of Biological Tissue Permittivity Data 115

Chapter 5 Microwaves in Biological Systems 119

5.1 Metrics for Exposure and Dosimetry 119
5.1.1 Exposure Quantities and Units 119
5.1.2 Dosimetry Quantities and Units 120

5.2 Reflection and Transmission at Planar Tissue Surfaces 122
5.2.1 Angle of Incidence and Polarization 125
5.3 Multiple Tissue Layers 125
5.4 Anatomic Phantom Models 129
5.4.1 SAR in Anatomical Models 130
5.5 Frequency Dependence and Resonance Absorption 132
5.6 Orientation and Polarization Effects for Elongated Bodies 136
5.7 Scattering Coefficient for Prolate Spheroidal Bodies............ 137
5.8 Doppler Effect from Target Motion...................................... 139
5.9 Range and Velocity Resolution... 141

Chapter 6 System Analysis and Signal Processing.. 145

6.1 Signals and Systems 145
6.1.1 Linear Systems 145
6.1.2 Orthogonal Signals.. 146
6.2 Fourier Series Representation of Signals 148
6.2.1 Example of Fourier Series Representation of Signals 149
6.2.2 Time Shifting and Scaling Properties of the Fourier Series 150
6.3 The Impulse Function as a Signal 151
6.3.1 Fourier Series for an Impulse Train 152
6.3.2 Sifting or Sampling Property of the Unit $\delta(t)$ Function... 153
6.4 Multiplication Property of Fourier Series 154
6.5 Impulse Response of a Linear System 155
6.6 Fourier Transforms.. 156
6.6.1 Fourier Transform Properties and Relations 156
6.7 Symmetry of Fourier Transforms... 160
6.8 System Transfer Function... 163
6.9 Sampling of Continuous Signals 163
6.9.1 Aliasing from Undersampling................................. 166
6.9.2 Quantization of Sampled Signals 166
6.10 Optimal Detection using Matched Filter.............................. 167
6.11 Cascaded Linear Systems and Filters................................... 169
6.11.1 An Ideal Low-Pass Inverse Filter 171
6.11.2 A Realistic Inverse Filter... 172
6.11.3 Distortionless Filter and System 174
6.11.4 Ideal High-Pass and Band-Pass Filters 176
6.11.5 A Practical Realizable Filter 177
6.12 Advanced Signal Conditioning and Processing Methods 178

Chapter 7 Vital Sign Sensing: Heartbeat and Respiration............................... 179

7.1 Organs in the Thorax... 180
7.1.1 The Heart and Coronary Vessels 180
7.1.2 The Lungs... 181

7.2 Measurement of Respiration ... 182
7.2.1 Respiratory Parameters ... 182
7.2.2 Microwave Measurement of Respiration ... 183
7.2.3 Respiratory Sensing of Animal Under Stress ... 186
7.2.4 Contactless Microwave Apnea Monitor ... 187
7.2.5 Other Developments in Microwave Respiratory Monitoring ... 190
7.3 Microwave Respiratory Sensor on A Chip ... 191
7.3.1 Doppler Radar Apnea Monitoring on a Single Chip ... 191
7.3.2 System-on-Chip Ultrawide-band Pulse Radar for Measuring Respiration Rate ... 193
7.3.3 Radar Measurement of Respiration During Cancer Radiotherapy ... 195
7.4 Continuous Respiratory Monitoring with Frequency-Modulated CW Radar ... 200
7.4.1 FMCW Radar Sensor ... 201
7.4.2 Preclinical Study Using a Prototype FMCW Sensor ... 202
7.5 Heartbeat Sensing and Microwave Cardiography ... 205
7.5.1 Measurement of MACG ... 208
7.6 Vital Sign Measurements ... 210
7.6.1 A Portable Contactless Vital-Sign Monitor ... 210
7.6.2 Remote Noncontact Vital-Sign Sensing ... 215
7.7 Recent Advances in Vital-Sign Sensing ... 222
7.7.1 Chip Scale Radar Sensors ... 223
7.7.2 Low-IF CW Radar Architecture and Injection-Locked Oscillators ... 228
7.7.3 Injection-Locked Oscillator Architectures ... 232
7.7.4 High Sensitivity CW Doppler CMOS Radar Chips ... 244
7.8 Summary and Perspective ... 260

Chapter 8 Arterial Pulse Wave and Pressure Sensing ... 266

8.1 The Circulatory System ... 268
8.2 Arterial Pulse-Wave Measurement ... 270
8.2.1 Noninvasive Contact Pulse-Wave Measurement ... 272
8.2.2 Near-Field Contactless Pulse-Wave Monitoring ... 280
8.3 Noninvasive Arterial-Pressure Sensing ... 287
8.3.1 Arterial-Wall Movement and Pressure Pulse ... 288
8.3.2 Doppler Radar Measurement of Pulse Pressure ... 288
8.3.3 Blood Pressure from PTT ... 291
8.3.4 SIL Microwave Radar Arterial Pressure Sensor ... 293
8.3.5 MMW Radar Pressure Sensor ... 296

8.4 Multiparameter Blood Pressure Sensing 300
8.5 Multipoint Near-Field Blood Pressure Sensing 300

Chapter 9 Sensing of Tissue Volume Change and Redistribution 307

9.1 Pathophysiologic Respiratory and Fluid Volume Changes 309
9.1.1 Pulmonary Edema and Pleural Effusion 310
9.1.2 Cerebral Edema 310
9.1.3 Arterial-Wall Movement and Blood Pressure 312
9.2 Microwave Sensing of Fluid Buildup in the Lungs 312
9.2.1 Earlier Pulmonary Edema Investigations 312
9.2.2 Wideband Microwave Scanning 315
9.3 Pulmonary Edema Diagnostic and Monitoring Systems 316
9.3.1 Body-Area Network-Integrated RF Sensor 317
9.3.2 Wideband Near-Field Microwave Detection 319
9.4 Commercial Wearable Sensing Systems 323
9.4.1 Wearable Near-Field RF Sensing System 323
9.4.2 Noncontact Near-Field Patch Sensor 324
9.5 Near-Field Respiratory Volume Sensing 327
9.6 Cerebral Edema and ICP 328
9.6.1 Microwave Transmission for Cerebral Edema in a Phantom Model 330
9.6.2 Microwave Sensing of Cerebral Edema in Animal Model 333
9.7 Microwave Tomographic Imaging of Hemorrhagic Head Phantom 339
9.8 Microwave Thermoacoustic Tomography and Imaging 340
9.9 Hemorrhagic Blood Volume Change 341

Chapter 10 Wearable Devices and Sensors 345

10.1 Fitness and Sleep Trackers 346
10.2 Smartwatch Heart-Rate Sensors 348
10.3 Wearable Microwave Vital-Sign Sensing 353
10.3.1 A Miniature Wearable Microwave Arterial Pulse Sensor 354
10.3.2 Wearable SILO Radar Pulse Sensors 356
10.3.3 Another Prototype Wearable Pulse Monitor 356
10.4 Wearable Microwave HR Sensors 358
10.5 Chest-Worn SILO Tag Sensor for HR Monitoring 360
10.6 Contact Sensing of Fingertip and Wrist Pulse Waves 364
10.7 Wearable Millimeter-Wave Arterial Pulse Sensor 368
10.8 Chest-Worn 5.8 GHz SILO for Respiration Monitoring 370
10.9 Wearable Cardiopulmonary Motion Sensors 373

Chapter 11 Advanced Topics and Contemporary Applications 379

11.1 Remote Radar Sensing of Vital Signs of Multiple Subjects 380

11.1.1 Detection of Subject Vital Signs Through Office Partitions 381

11.1.2 Contactless Heart Rate Measurement Using X-Band Array Radar 384

11.1.3 Hybrid Doppler Radars for Multisubject Vital-Sign Sensing 386

11.1.4 Sensors for Localization of Multiple Subjects in Cluttered Environments 392

11.1.5 Software Algorithm-Assisted 24 GHz FMCW Radar Sensing 405

11.1.6 MM-Wave Radar Sensor for Multiple Subjects........ 418

11.2 Applications in Medicine and Healthcare 423

11.2.1 Sleep Medicine — Diagnosis of Sleep Apnea-Hypopnea Syndrome 423

11.2.2 Real-Time Apnea-Hypopnea Event Detection 427

11.2.3 Postsurgery and Anesthesia Recovery 430

11.2.4 Monitoring Diabetes-Related Physiological Signals 432

11.2.5 Telehealth and Telemedicine for Diabetes Management 436

11.3 Monitoring Driver Vital Signs 438

Appendix 449

Index 451

List of Figures and Tables

Figure 1.1 A part of the electromagnetic spectrum including microwave and radio frequency radiation. 3

Figure 1.2 The sine wave, sin (*t*), and definition of a wavelength, λ. 4

Figure 1.3 Active and passive modalities for noninvasive microwave sensing of physiological changes and conditions........ 8

Figure 1.4 Basic functional diagram of a Doppler microwave physiological sensor. 9

Figure 1.5 Frequencies for minimal attenuation of microwave signals and maximal spatial resolution in skin (muscle) and fat tissues. 13

Figure 1.6 System setup of a Doppler microwave radar system for vital-sign measurement. 14

Figure 2.1 A basic functional diagram of a Doppler microwave physiological sensor. 35

Figure 2.2 Microwave measurement of respiration of an unanesthetized but calm rabbit inside of a cardboard box. 36

Figure 2.3 Microwave respiratory measurement for a seated human subject breathing at 47 times per minute. 37

Figure 2.4 A transceiver horn antenna directed microwaves at 10 GHz toward the upper torso of the cat. 37

Figure 2.5 A microwave apnea detector recorded respiratory activity of an anesthetized cat showing apneic episode and recovery. 38

Figure 2.6 Continuous tracing of microwave sensor-monitored respiratory record of a cat subjected to a brief period (heating on and off) of selective heating of the head and brain. 38

Figure 2.7 A human participant lying on a table in the supine position. 39

Figure 2.8 Microwave apexcardiography or Doppler radar sensing of a healthy young male participant's cardiac events. 40

Figure 2.9 Changes in the baseline of the amplitude of the microwave reflection coefficient and in left atrial pressure during development of pulmonary edema in an anesthetized 25 kg dog on a respirator. 42

Figure 2.10 A microprocessor-based contactless 10.5 GHz microwave vital sign monitor showing a circuit board and handheld circularly polarized antenna. 44

Figure 2.11 Heart and respiration channel records of a healthy human subject from a microprocessor-based contactless 10.5 GHz microwave vital sign monitor. 44

Figure 2.12 Contactless remote microwave sensing of vital signs of a human subject wearing summer or winter clothing. 45

Figure 2.13 Microwave (20 mW, 10 GHz) sensing of heartbeat and respiration from a human subject sitting behind a cinder block wall (15 cm thick) at 3 m. 46

Figure 2.14 Heartbeat and respiration signals of a female human subject recorded from the top of simulated rubble with a 450 MHz reflector antenna. The subject is lying within a cavity among the rubble. The peak at 0.6 Hz is the second harmonic of the respiration signal........ 46

Figure 2.15 A direct contact Doppler microwave arterial pulse wave sensor. 47

Figure 2.16 Oscilloscope tracings of brachial artery motion measured using a 25 GHz Doppler microwave sensor in contact with the skin on the arm over the artery........ 48

Figure 2.17 Tracings of arterial-wall motion measured using 10 GHz Doppler microwaves: (a) radial artery in the arm; (b) femoral; (c) posterior tibial; and (d) dorsalis pedis arteries in the leg of a human subject. 48

Figure 2.18 Microwave sensing of the carotid pressure pulse wave (MWPP) and invasively recorded intra-aortic pressure pulse wave (IAPP) from a human subject........ 49

Figure 2.19 Microwave sensing of intracranial pressure (ICP) in rats. Maximum phase change versus ICP change for injections of aliquots (symbols represent volume of aliquots)........ 50

Figure 2.20 Intracranial pressure (ICP) in rats (bottom), electrocardiogram (ECG) (middle), and microwave phase change (top) following aliquot injection of 0.07 and 0.05 mL aliquots of saline (arrows). 51

Figure 3.1 Boundary conditions and schematics for evaluating tangential and normal electric and magnetic field components at interface between two different material media. (a) tangential components of the electric field strength; (b) Normal components of the electric flux density; (c) Tangential components of magnetic field strength; (d) Normal components of magnetic flux density........ 64

Figure 3.2 The direction of plane-wave propagation, electric field, and magnetic field orientation in space at a given moment in time. 67

Figure 3.3 Polarization of electromagnetic plane waves: (a) linear polarization; (b) circular polarization; (c) elliptical polarization. Arrows indicate directions of electric field and its coordinate components. ... 68

Figure 3.4 A standing wave created when a plane wave impinges normally on a perfect conductor. The fields are shown at time, t = T/8, where T is the period of the wave. ... 72

Figure 3.5 Plane wave impinging on two-layered media: medium 1 (air) and medium 2 (a tissue layer). ... 72

Figure 3.6 Plane wave incident upon a boundary surface at an angle of incidence θ. ... 75

Figure 3.7 An elementary dipole antenna of length l which is short compared with a wavelength, ($\lambda \gg l$), and the width or diameter is small compared with its length. ... 77

Figure 3.8 Flow of electromagnetic energy from a dipole antenna where the arrows represent the direction of energy flow at successive instants of time. The same flow pattern is on both sides of the dipole antenna. ... 79

Figure 3.9 The on-axis power density of a uniform square antenna. ... 81

Figure 3.10 The on-axis power density of a tapered circular aperture antenna. ... 81

Figure 3.11 An 3-D sketch of a donut shaped or toroidal radiation pattern for a typical linear dipole antenna with its length along the z-axis. ... 85

Figure 3.12 Configuration for open-ended waveguide (a) and rectangular horn (b) antenna: (A and a) and (B and b) indicating width and height of horn and waveguide sections, respectively. ... 85

Figure 3.13 Shape of circular dish and parabolic reflector antennas. ... 85

Figure 3.14 Photograph of a cavity-backed microwave slot antenna. ... 86

Figure 3.15 Schematic diagram of a circular or parabolic reflector antenna. ... 86

Figure 3.16 Radiation pattern for a circular dish antenna with a main and multiple minor or side lobes. ... 87

Figure 3.17 Radiation pattern for a horn antenna with main and side lobes. ... 87

Figure 3.18 A coaxial circular waveguide aperture antenna. ... 88

Figure 3.19 A 2450 MHz aperture antenna with circular matching dielectric plate for direct-contact applications. ... 88

Figure 3.20 The design of a 4 × 4 element patch antenna array. 89

Figure 3.21 Patch antenna arrays with 2 × 1 elements (a), 3 × 2 elements (b); and 6 × 2 -elements (c). Dimensions in millimeters.................. 89

Figure 3.22 Simulated 3-D far-field patterns (FFP) of patch antenna arrays shown in Figure 3.21(a), (b), and (c). (From Rabbani and Ghafouri-Shiraz, 2017.)... 90

Figure 3.23 A prototype dual-band wearable button antenna sensor. 91

Figure 3.24 Design configuration of circularly polarized patch antenna: $r_{i1} = 6$ mm, $r_{o1} = 7.5$ mm, $r_{i2} = 10.5$ mm, $r_{o2} = 13$ mm, $g_1 = 1$ mm, $g_2 = 8$ mm, $\theta_1 = 45°$, $\theta_2 = 157.5°$, $r_u = 10$ mm, $r_1 = 4$ mm, $l_f = 10$ mm, $w_f = 1.5$ mm, $l = 45$ mm, $w = 34$ mm, $t_s = 0.8$ mm, and $t_c = 27 \mu$m. 91

Figure 3.25 Simulated performance of circular polarized patch antenna with and without the outer ring slot shown in Figure 3.22: (a) S11 transmission parameter, (b) axial ratio parameter, (c) E-plane radiation pattern, and (d) H-plane radiation pattern. 92

Figure 4.1 Dielectric permittivity and electrical conductivity of muscle-like biological materials as a function of frequency from 1 Hz to 1 THz. 95

Figure 4.2 Frequency dependence of permittivity of typical or common low-loss dielectric materials. 97

Figure 4.3 Frequency-dependent characteristics of permittivity and conductivity of lossy dielectric materials. 100

Figure 4.4 Temperature dependence of relative permittivity and conductivity of animal liver tissue at 2450 MHz. 104

Figure 4.5 Permittivity (dielectric constant and conductivity) of free water at 37 °C from 0.01 to 1000 GHz (10 MHz to 1 THz). 105

Figure 4.6 Temperature dependence of dielectric permittivity (dielectric constant and conductivity) at six microwave frequencies. 106

Figure 4.7 Dielectric permittivity and conductivity of gray matter in the brain at 37°C. (From Gabriel and Gabriel, 1996.) 109

Figure 4.8 Dielectric permittivity and conductivity of white matter in brain at 37°C. (From Gabriel and Gabriel, 1996.) 109

Figure 4.9 Permittivity properties of homogenized fresh brain tissues at 37°C in the microwave frequency range 2–4 GHz. Fresh human data (a) and combined fresh canine, ovine, primate, swine, and human (b)... 110

Figure 4.10 Dielectric constant ε_r and conductivity σ for blood at 37°C as a function of frequency. (From Gabriel and Gabriel, 1996.) 111

Figure 4.11 Relative permittivity and conductivity for the heart muscle in the frequency range of 10 Hz to 100 GHz. (From Gabriel and Gabriel, 1996.) 112

Figure 4.12 Relative permittivity and conductivity for the aorta in the frequency range of 10 Hz to 100 GHz. (From Gabriel and Gabriel, 1996.) 112

Figure 4.13 Frequency dependence of the dielectric constant and conductivity for deflated lungs. (From Gabriel and Gabriel, 1996.) 113

Figure 4.14 Frequency dependence of the dielectric constant and conductivity for inflated lungs. (From Gabriel and Gabriel, 1996.) 114

Figure 4.15 Relative permittivity and conductivity for cerebrospinal fluid tissues in the frequency range of 10 Hz to 100 GHz. (From Gabriel and Gabriel, 1996.) 114

Figure 4.16 Dielectric permittivity and conductivity for fat tissues in the frequency range of 10 Hz to 100 GHz. (From Gabriel and Gabriel, 1996.) 115

Figure 4.17 Measured and modeled tissue properties using two Debye relaxation constants for (a) muscle and (b) fat. 116

Figure 5.1 A plane wave impinging normally on a planar tissue medium. 122

Figure 5.2 Power transmission coefficients at different tissue interfaces as functions of frequency. The power reflection coefficient is equal to 1 – the power transmission coefficient. 124

Figure 5.3 Magnitude of reflection coefficients for E and H polarized microwaves at 2450 MHz with a plane wavefront. 126

Figure 5.4 Phase of reflection coefficients for E and H polarized 2450 MHz microwaves with a plane wavefront. 126

Figure 5.5 Plane wave in air impinging on a composite fat-muscle layer. 127

Figure 5.6 Relative specific absorption rate in planar fat-muscle layers. 128

Figure 5.7 The peak specific absorption rate as a function of fat-layer thickness in a planar layered tissue model of skin-fat-muscle at different frequencies. The skin thickness is 2 mm, and the incident power density is 10 W/m^2. 129

Figure 5.8 Normalized amplitudes in and outside the horizontal section of a phantom head model exposed to microwave radiation. (From Mobashsher et al., 2016.) 131

Figure 5.9 Plane wave specific absorption rate distribution in the central coronal section of a human body model at three microwave frequencies: (a) 700 MHz; (b) 1800 MHz; (c) 2700 MHz normalized to 1 W/kg (0 dB). 132

Figure 5.10 Frequency and size dependence of absorption in a 14-cm diameter spherical model of the human brain and muscle equivalent materials from 100 MHz to 10 GHz. 133

Figure 5.11 Specific absorption rate distribution in a homogeneous spherical brain model (18 cm diameter) exposed to a 915 MHz plane wave. The direction of microwave propagation is along the z axis. 133

Figure 5.12 Specific absorption rate characteristics in 2-D displaying microwave absorption in the canonical brain models exposed to 915 MHz plane waves propagating along the x direction. Note symmetry in the transverse dimension. 134

Figure 5.13 Specific absorption rate distributions inside a 9-cm radius adult brain sphere exposed to a 400 MHz plane wave. The three rows represent XY, ZX, and YZ plane patterns, respectively. The corresponding line distributions are along the direction of propagation (red) and transverse (blue) to the direction of propagation shown on the right. The direction of wave propagation is along the X axis. 135

Figure 5.14 The scattering coefficient for a 14-cm long homogeneous prolate spheroidal tissue model with a major-to-minor axis ration of 1.5 exposed to a 915 MHz plane wave. 137

Figure 5.15 The scattering coefficient for a 14-cm long homogeneous prolate spheroidal tissue model with a major-to-minor axis ration of 1.5 irradiated by 2450 MHz microwaves. 138

Figure 5.16 Scattering of a plane wave by a moving biological target with velocity, *u*. 139

Figure 5.17 Effect of target rotation on reflected microwave signal. 140

Figure 6.1 A periodic sequence of rectangular t_0 wide pulses with a period of T. 149

Figure 6.2 The impulse function. 152

Figure 6.3 An impulse train, $f(t) = \delta(t)$ with a period, T. 153

Figure 6.4 The spectrum of Fourier series for an impulse train. 153

Figure 6.5 The input $f(t)$ and output $g(t)$ of a linear system $h(t)$ in block diagram form. 155

Figure 6.6 An illustration of the symmetry of Fourier transform pairs: (a) rect (t), (b) Fourier transform of rect (t), spectrum with constant over a specific frequency band and zero elsewhere, and (d) time function or inverse transform of (c). 161

Figure 6.7 The system transfer function for a generalized linear system......... 163

Figure 6.8 An impulse train: comb function.. 164

Figure 6.9 Block diagram representation of two cascaded systems in time domain. 170

Figure 6.10 Block diagram for a cascaded system with an ideal low-pass inverse filter. 171

Figure 6.11 Normalized Gaussian impulse response function where $1/\sqrt{2}a$ is half-pulse width. 172

Figure 6.12 System transfer function (spectral distribution) of a Gaussian pulse with a half-pulse width, $1/\sqrt{2}a = 1\mu s$. 173

Figure 6.13 An inverse filter, $H_2(\omega)$ with ω_{max} cutoff to realize an ideal low-pass inverse filter, $H(\omega) = H_1(\omega)\, H_2(\omega)$ with ω_{max} cutoff. 174

Figure 6.14 Amplitude and phase response of $A_0\, e^{(-j(\omega t_0))}$ of a distortionless system. 175

Figure 6.15 Ideal high-pass filter characteristics. 176

Figure 6.16 The system transfer function for an ideal band-pass filter.............. 177

Figure 6.17 Frequency response of a 12th-order elliptic infinite impulse response filter to separate the heart signal from a signal that includes both heart and respiration information............................ 177

Figure 7.1 Anatomic structure of the human heart and its position in the thorax. 180

Figure 7.2 The lungs within the human chest and rib cage. 182

Figure 7.3 Block diagram of a continuous wave microwave radar sensor for respiration. Note that received microwave signal is mixed or compared with a portion of the transmitted microwave serving as a reference signal at the same frequency, the result is a baseband signal. The scheme is called homodyne detection...... 184

Figure 7.4 Measurements of respiratory movement of an intact (unanesthetized) rabbit: upper tracing for microwave sensing; lower tracing for anemometer. 185

Figure 7.5 Respiratory measurement from a human subject: upper tracing for microwave; lower tracing for anemometer.................... 186

Figure 7.6 A continuous wave microwave sensor monitored respiratory record (uninterrupted from a-f) of a cat subjected to a brief period of selective heating of the head (see heating on and off arrows)....... 187

Figure 7.7 A contactless microwave apnea monitor. 188

Figure 7.8 A microwave apnea detector recorded respiratory activity of an anesthetized cat showing apneic episode and recovery......... 189

Figure 7.9 Functional block diagram of a single-chip quadrature radar transceiver.......... 192

Figure 7.10 Architecture and photograph of single chip quadrature Doppler radar transceiver for noncontact physiological sensing. (Courtesy of Jenshan Lin, University of Florida and Bell Laboratories.) 192

Figure 7.11 System diagram of SoC UWB pulse radar (a). The dashed lines around the target indicate the range spanned by the radar in ranging (RM) and tracking (TM) modes. Representation of the pulses at the input and output of the multiplier for three different cases of relative shift between the input pulses (b). Representation of the input and output voltages of the integrator for stationary and moving targets (c). 194

Figure 7.12 Output from PG of the SoC radar: (a) Ultrawide-band (UWB) pulses with 350 ps duration; (b) The power spectral density (PSD) of pulse measured before and after antenna filtering and FCC UWB masking.......... 195

Figure 7.13 Input (upper trace) and output (lower trace) signals of the multiplier measured for three cases: (a) monocycle input pulses without relative delay (i.e., time alignment), (b) a relative delay of half of the time duration, and (c) relative delay equal to the time duration. 196

Figure 7.14 System on chip ultrawide-band pulse radar. Micrograph of the radar chip (a). The die size is 1.5 × 1.3 mm (including the multiplier as stand-alone device). Radar testchip packaged in a leadless package (bottom view) with exposed ground pad (size 5 × 5 mm) (b).......... 196

Figure 7.15 Respiration record of a seated female detected with ultrawide-band radar sensor at 30 cm in front of chest. The measured output voltage in TM mode (fPR at 40 MHz) is expressed in mV and shows a respiratory rate about 0.3 Hz. 197

Figure 7.16 Output voltage (mV) showing respiratory record of a male subject from before and after voluntarily holding his breath at 25 cm from the radar. 197

Figure 7.17 Motion-adaptive radiotherapy based on radar respiration sensing. The process includes two steps: treatment planning and treatment execution sessions. Insets: (a) multiple radars, (b) beam-scanning radar, and (c) the 2.4-GHz miniature radar sensor (see quarter coin for size comparison). (Courtesy of Changzhi Li, Texas Tech University.).......... 198

Figure 7.18 Block diagram of DC-coupled radar sensor system with RF coarse-tuning and baseband fine-tuning architectures. ZigBee protocols are used to transmit data and receive commands wirelessly. (Courtesy of Changzhi Li, Texas Tech University.) 199

Figure 7.19 DC-coupled sensor measured respiratory signal of a human participant: (a) Radar measured respiration signal; (b) Generated gating signal. The shaded area indicates the coach reference data domain, and the line represents the reference for gating. 200

Figure 7.20 Transmitted waveform of a sawtooth frequency-modulated continuous wave (FMCW) radar: Ramp frequency modulation versus time (upper) and instantaneous amplitude variation with time (lower). 201

Figure 7.21 Photograph of prototype quadrature frequency-modulated continuous wave radar showing signal generator and patch array antennas with low-noise amplifier (LNA), data acquisition (DAQ), and local oscillator (LO). (Courtesy of Changzhi Li, Texas Tech University.) 203

Figure 7.22 Human respiration pattern showing chest-wall displacement obtained using a 5.8 GHz frequency-modulated continuous wave radar sensor. 203

Figure 7.23 Frequency-modulated continuous wave radar-detected patient breathing patterns with superimposed heartbeats during mechanical ventilation. 204

Figure 7.24 Frequency-modulated continuous wave radar monitored spontaneous breathing with different breathing patterns. Each inspiratory cycle is characterized by a first peak (chest-wall expansion during inhalation) followed by a curved peak (during exhalation). 205

Figure 7.25 The sternum, xiphoid, and thoracic cage. 206

Figure 7.26 Antenna located over the apex of the heart for microwave apexcardiography. 207

Figure 7.27 Illustration of electrocardiography (ECG), apexcardiography (ACG), and microwave apexcardiography (MACG) recordings in arbitrary units. 207

Figure 7.28 Experimental diagram for microwave cardiography - noncontact microwave measurement of precordial movements using homodyne detection. 208

Figure 7.29 Microwave pulsatile microwave apexcardiography (MACG) for a healthy young male along with electrocardiography

(ECG) and phonocardiography (PCG) tracings. Note the same heart rate is recorded by the ECG, PCG, and MACG. 209

Figure 7.30 Salient features (landmarks) of microwave-measured ventricular movement in a healthy young male. 209

Figure 7.31 Functional diagram of a portable contactless vital sign monitor. 211

Figure 7.32 Transceiver output signal sensed from human chest. 212

Figure 7.33 Typical heart and breathing waveforms recorded by the portable contactless vital sign monitor from a healthy young adult. 212

Figure 7.34 Scatter plot of measured and visually identified breathing rates of rats. 213

Figure 7.35 Scatter graphs of the vital-sign monitor displaying measured and visually identified heart (a) and respiration rates (b) for human subjects. 214

Figure 7.36 Summary of basic steps in the pattern recognition software algorithm. 214

Figure 7.37 Schematic diagram of the remote heart and respiration rate detection system. 216

Figure 7.38 Microwave sensing of heartbeat and respiration from a human subject sitting at 2 m from and behind a 15 cm thick cinder block wall. 217

Figure 7.39 Heart signals of a human subject lying on the ground at 30 m measured with a 10 GHz microwave Doppler radar beam. 217

Figure 7.40 Schematic diagram of a 1150-MHz microwave life-detection system. 219

Figure 7.41 Heartbeat and respiration signals of a female human subject recorded from the top of simulated rubble with a 450 MHz reflector antenna. The subject is lying within a cavity in the rubble. The peak at 0.6 Hz is the second harmonic of the respiration signal. (a) Temporal waveform, (b) frequency spectrum. 220

Figure 7.42 Breathing and heartbeat signals recorded from a human subject lying beneath 9 ft (~2.74 m) of rubble by a 450 MHz life-detection system. (a) Temporal waveform, (b) frequency spectrum.. 221

Figure 7.43 Sensing of heartbeat signals by two side-by-side antennas in a 1150 MHz life-detection system. Simulation of human subjects or a phantom heart model under 3 ft of wire-mesh rubble. ... 221

Figure 7.44 Phantom heartbeat signals sensed by two side-by-side antennas in a 1150 MHz life-detection system. Results are displayed as time-domain, spectra (FFT), and cross correlations. ... 222

Figure 7.45 Heart and respiration activity measured with the 2.4 GHz quadrature radar chip. The analog filtered I and Q outputs, which contain both heart and respiration information, are shown at the top, followed by the digitally filtered I and Q signals, with only heart information. Neither the I nor Q output is at the maximum sensitivity point or at the null point. They have similar amplitudes and accuracies. The I output is within 1 beat per min of the reference 82% of the time, and the Q output is correct 81% of the time. ... 224

Figure 7.46 Heart and respiration activity measured with the 1.6 GHz BiCMOS chip. The top trace is the analog-filtered raw signal, and the second is the analog-filtered heart signal. The third and fourth traces are the raw and heart signals, respectively, after digital filtering. The bottom trace is the pulse reference. The filtered heart signal was within one beat per minute of the reference 100% of the time, while the filtered raw signal agreed 92% of the time. ... 225

Figure 7.47 Schematic diagram of the 5 GHz radar transceiver with interfaces for input/output antennas. (Courtesy of Changzhi Li, Texas Tech University.) ... 226

Figure 7.48 Photomicrograph of integrated chip sensors: (a) a double sideband vital-sign detection radar fabricated in 0.18 μm CMOS process (Li et al., 2008) and (b) a direct conversion radar fabricated in 0.13 μm CMOS process. (Courtesy of Changzhi Li, Texas Tech University.) ... 226

Figure 7.49 Schematic block diagram of the software-configurable 5.8 GHz quadrature continuous wave radar-on-chip sensor. (Courtesy of Changzhi Li, Texas Tech University.) ... 227

Figure 7.50 Radar-on-chip output signal detected from the back of a human subject: Waveforms of I (dashed line) and Q (solid line) channels (top) and frequency spectrum of demodulated (CSD) signal (bottom). ... 227

Figure 7.51 CMOS radar-on-chip sensor output signal detected from the front of a human subject at 1.5 m: Waveforms of I (dashed line) and Q (solid line) channels (top) and frequency spectrum of demodulated (CSD) signal (bottom). ... 228

Figure 7.52 Schematic diagram of coherent low-IF system showing signal flow. 229

Figure 7.53 Schematic diagram of a 5.8 GHz double-sideband low-IF continuous wave radar system with both envelope detection (ED) and synchronous demodulation (SD) demonstrated at the output. 230

Figure 7.54 Experimental setup for motion measurements using the 5.8 GHz low-IF radar system with a pair of 2 × 2 patch antennas for microwave transmission and reception. The human subject would be in the position of actuator and metal plate shown. (Courtesy of Lianming Li, Southeast University.) 231

Figure 7.55 Comparison between the envelop detection and synchronous demodulation methods for vital sign detection. The 20-s waveform (a-top) and corresponding power spectrum under normal (freely) breathing conditions (b-bottom). 231

Figure 7.56 Prolonged human vital-sign (heartbeat) monitoring by envelope detection (ED) method. The total detection interval is 140 s. Detected vital-sign (heartbeat) results are the same as the reference pulse rate. The detection accuracy is better than 96%. 232

Figure 7.57 Schematic diagram of a self-injection-locked oscillator (SILO) radar system 233

Figure 7.58 Schematic diagram of an SIL radar sensor developed for vital-sign measurement using an ISM band. It includes annotated specifications of key system components. 233

Figure 7.59 Vital signs detected using ISM band SIL radar: Breathing waveform (top) and frequency spectrum showing a rate of 17 beats/min (below). 234

Figure 7.60 Heartbeat detected using an ISM SIL radar sensor: (a) Heartbeat waveform and (b) Frequency spectrum indicating a heartbeat of 79 beats/min. 235

Figure 7.61 Heart signal detection results at different distances between the subject and SIL sensor operating at 1.8 GHz. 236

Figure 7.62 Heart signal detection results at different distances between the subject and SIL sensor operating at 2.4 GHz. 237

Figure 7.63 Heart signal detection results at different distances between the subject and SIL sensor operating at 3.6 GHz. 238

Figure 7.64 Heart signal detection using an SIL sensor at a continuous wave Doppler radar "null" point showing heart-signal detection with frequency sweeping compared to that without. 238

Figure 7.65 SIL AIA radar sensor: (a) Circuit diagram of self-oscillating AIA sensor, (b) Photograph of AIA, and (c) Schematic diagram showing differentiator-based envelop detector. (Courtesy of Chao-Hsiung Tseng, National Taiwan University of Science and Technology.) 239

Figure 7.66 SIL AIA sensor measurement of a cardiopulmonary signal: (a) Time-domain results of cardiopulmonary detection and (b) Spectrum showing respiration and heartbeat rates. Inset: Reference pulse rate from finger. 240

Figure 7.67 Schematic and timing diagram of the frequency modulated SIL radar architecture. 241

Figure 7.68 Experimental arrangement for remote SIL radar detection of location and cardiopulmonary signatures: (a) Photograph of two subjects seated 2–5 m behind a wooden partition wall and (b) Reconstructed image of subject locations. (Courtesy of T.S. Jason Horng, National Sun Yat-Sen University.) 241

Figure 7.69 Schematic diagram of single-conversion SIL (SCSIL) hybrid mode radar sensor. 242

Figure 7.70 Experimental arrangement for remote single-conversion SIL (SCSIL) radar detection and sensing of the vital signs of two seated subjects. (Courtesy of Fu-Kang Wang, National Sun Yat-Sen University.) 243

Figure 7.71 Experimental results obtained using fast Fourier transform (FFT) and frequency estimation algorithms (FEA). The black and gray lines with circular symbols represent the output spectra of the baseband signals: (a) Range detection and (b) Vital-sign detection. 244

Figure 7.72 Photograph (a) and schematic diagram (b) of a 60 GHz prototype vital-sign measurement system setup using V-band waveguide components. (Courtesy of Tzuen-Hsi Huang, National Cheng Kung University.) 246

Figure 7.73 System block diagram illustrating CMOS Doppler radar, flip-chip integration, TX and RX PCB patch antennas, 60 GHz RF section, 6 GHz IF, and baseband I/Q outputs. The overall dimensions are 31.3 × 45 mm. 247

Figure 7.74 Photomicrograph of the 60 GHz CMOS radar chip. (Courtesy of Jenshan Lin, University of Florida.) 247

Figure 7.75 Final system photograph including the flipped chip, TX and RX patch antennas, and DC bias wires. (Courtesy of Jenshan Lin, University of Florida.) 248

Figure 7.76 Spectrum of respiration signal detection from two different displacements: (a) No prominent respiration peak and (b) possible respiration peak at 15 breath/min. 248

Figure 7.77 60 GHz CMOS radar chip detected respiration signals: (a) I and Q outputs before recovery algorithm is applied and I and Q outputs after recovery algorithm is applied and (b) spectrum of recovered respiration peak from I and Q outputs for the signal shown in Figure 7.76(a). 249

Figure 7.78 Photomicrograph of 60 GHz CMOS direct-conversion Doppler radar chip (size 2 × 2 mm). (Courtesy of Huey-Ru Chuang and Tzuen-Hsi Huang, National Cheng Kung University.)..250

Figure 7.79 Schematic diagram of 60 GHz CMOS direct-conversion Doppler radar RF sensor with clutter canceller circuits for single-antenna noncontact human vital-signs detection. The Doppler radar chip sensor has a high isolation QC and a clutter canceller circuit. It consists of a VCO, FD, PA, and QC, clutter canceller with a low phase-variation VGA and a full 360 continuously adjustable PS, LNA, I/Q subharmonic mixer (SHM), and three directional couplers. The inset figure to the right illustrates the principle of clutter cancellation. (Courtesy of Tzuen-Hsi Huang, National Cheng Kung University.)...251

Figure 7.80 Measured respiration and heartbeat signals of the human subject at 0.75 m: (a) Time-domain I/Q signal of the heartbeat signal, (b) Frequency spectrum of the heartbeat signal, (c) Time-domain I/Q signal of the breathing signal, and (d) Frequency spectrum of the respiration signal. 253

Figure 7.81 Photomicrograph of 60 GHz CMOS Doppler radar sensor integrated with a V-band PD. The chip size is 2 × 2.34 mm. (Courtesy of Huey-Ru Chuang, Tzuen-Hsi Huang, National Cheng Kung University.)...254

Figure 7.82 V-band Doppler radar-measured respiration and heartbeat signals of the human subject with normal breathing at 1.2 m: (a) Time-domain I/Q channel signals and (b) Frequency spectrum. 255

Figure 7.83 V-band radar sensor measured heartbeat signals of a human subject holding its breath at 1.2 m: (a) Time-domain I/Q channel signals and (b) Frequency spectrum. 256

Figure 7.84 Photomicrograph of 65 nm CMOS 100 GHz radar system on chip with dimensions of 0.9 × 2.0 mm including circuit blocks: LNA, I/Q down-conversion mixer, polyphase filter

(PPF), IF transimpedance amplifier (TIA), LO generation, up-conversion mixer, and power amplifier (PA) and surrounding test pads. (Courtesy of Lianming Li, Southeast University.) 256

Figure 7.85 Schematic diagram of the 100 GHz double-sideband low-IF continuous wave Doppler radar system-on-chip with transceiver chip, two horn antennas, and the off-chip digital signal processing. (Courtesy of Jenshan Lin, University of Florida.) 257

Figure 7.86 Human vital-sign detection results from 2 m: (a) Two segments of time domain signals detected with and without respiration, (b) Normalized spectrum distribution showing breathing and heartbeat rates with respiration, and (c) spectrum distribution showing heart rate without respiration. 258

Figure 8.1 Tracing of an arterial pulse wave illustrating the location of the foot, the systolic peak, and the dicrotic notch in the pulse waveform. 267

Figure 8.2 Major blood vessels near the heart. 268

Figure 8.3 Major arteries of the head and neck. 269

Figure 8.4 Arteries in the arm and shoulder. 270

Figure 8.5 Arterial and veinous circulation of the leg. 271

Figure 8.6 Functional diagram of a contact Doppler K-band radar arterial pulse-wave sensor and analyzer. 272

Figure 8.7 A contact Doppler K-band radar arterial pulse-wave sensor and analyzer with 1 × 1 cm waveguide antenna applicator. 273

Figure 8.8 Arterial pulse waveforms detected by the K-band Doppler pulse-wave sensor: (a) carotid pulse, (b) radial pulse, and (c) brachial pulse. 274

Figure 8.9 Similarity of radial pulse waveform for the same subject: (a) Initial recording and (b) recording taken 4 months later. 274

Figure 8.10 Recordings of the radial pulse made at three test distances by the same microwave sensor: (top) 0.6 cm, (middle) 1.3 cm, and (bottom) 2.5 cm were used for the measurements. 275

Figure 8.11 Feature extraction algorithm for analysis of arterial pulse wave patterns. 276

Figure 8.12 Microwave-sensed pulse waves from peripheral arteries in the human upper and lower extremities: (a) Radial in the arm, and (b) femoral, (c) posterior tibial, and (d) dorsalis pedis arteries in the leg. 277

Figure 8.13 Schematic diagram of a compact S-band microwave arterial pulse-wave sensor. The ribbon antenna is seen at the upper right corner within the transistor circle. (Lin, 1989.)...................... 278

Figure 8.14 A compact S-band microwave sensor held by an elastic headband for direct contact with the skin over the temporal region of the head. 279

Figure 8.15 A compact S-band microwave sensor measured superficial temporal artery pulse waves by direct contact with the scalp..........279

Figure 8.16 Schematic diagram of the proposed self-injection locked radar architecture for a wrist pulse rate sensor.............................. 280

Figure 8.17 Photograph of wrist pulse rate monitor attached through clothing with a wristband. (Courtesy of Fu-Kang Wang, National Sun Yat-Sen University.) 281

Figure 8.18 Radial pulse detected through a sleeved shirt from a subject: (a) Bandpass-filtered pulse signal and (b) frequency spectrum. 282

Figure 8.19 Schematic diagrams for a wrist pulse detection (a) and microwave sensor based on injection- and phase-locked loop (PLL) (b). 282

Figure 8.20 Injection and phase-locked loop sensor-measured wrist pulse signal: (a) Time-domain bandpass-filtered signal from sensor, (b) frequency spectrum from radar sensor, and (c-bottom) bandpass-filtered data and frequency spectrum from piezoelectric transducer. 283

Figure 8.21 Wearable self-injection locked radar pulse rate sensor with amplifier integrated antenna (AIA) and differentiator-based envelope detector. 284

Figure 8.22 Self-injection locked radar measured pulse-wave data: (top) Time-domain results of wrist pulse detection and (bottom) normalized spectrum. 285

Figure 8.23 Image of a frequency-modulated continuous wave mm-wave radar chip showing transmitter and receiver locations. (Courtesy of Jessi Johnson, Blumio, Inc.)...................................... 286

Figure 8.24 Normalized time-domain waveform (top) and frequency spectrum (bottom) measured from the radial artery of a human subject. 287

Figure 8.25 Comparison of simultaneous intra-aortic pressure pulse (IAPP) and noninvasive microwave (MWPP) pulse pressure sensing. 289

Figure 8.26 Analysis of pulse wave diagnostic features: QS2 (Q wave to second heart sound time), LVET (Left Ventricular Ejection Time), PEP (Pre-Ejection Period) = QS2 – LVET......................... 290

Figure 8.27 Method of pulse transit time extraction from aortic and radial pulse waves measured by a microwave sensor. 292

Figure 8.28 Handheld self-injection locked radar arterial pulse pressure wave sensor. (Courtesy of Chao-Hsiung Tseng, National Taiwan University of Science and Technology.) 294

Figure 8.29 Definition of S1, the first systolic peak and S2, second systolic peak of the arterial pulse wave and R-PTT, the time interval between S1 and S2. 294

Figure 8.30 Photographs of near-field microwave self-injection locked (NFSIL) radar sensor with a split-ring resonator, amplitude demodulator, and MCU module. (Courtesy of Chao-Hsiung Tseng, National Taiwan University of Science and Technology.) 295

Figure 8.31 Self-injection locked oscillator radar sensor measured raw (top) and filtered (bottom) arterial pulse waveforms from the wrist of normal subject. 295

Figure 8.32 Frequency-modulated continuous wave mm-wave radar sensor in a plastic cover attached to the subject using a nylon strap and placed over the radial artery (a). Simultaneous recordings of radial arterial pressure waves using a handheld tonometer on the opposite wrist (b). (Courtesy of Jessi Johnson, Blumio, Inc.) 297

Figure 8.33 Example waveforms and corresponding spectral distribution for subjects with varying R2 values: (a) low, P9; (b) typical, P3; and (c) high, P12, obtained by mm-wave radar and tonometer (dotted line). 298

Figure 8.34 Prototype multipoint near-field sensing system: (a) The transceiver by two software-defined radios (SDR1 and SDR2), (b) the sensing antenna pair at 1.8 GHz band, (c) the 900 MHz and 5 GHz bands, and (d) the sensing antenna placement when four antenna pairs are deployed to Points 1–4. The sensing antenna pairs are placed over the shirt. (Hui et al., 2020.) 301

Figure 8.35 The multipoint microwave system for near-field sensing. Placement of the sensing points (1–4): 0 (Erb's point), ST (stethoscope), LL and RA (ECG electrodes). (Hui et al., 2020.) 302

Figure 8.36 Central blood pressure analysis based on Hilbert-Huang transform frequency-time analysis of near-field backscattering channel C11 during systole: (Top) Subject sat on the floor; (bottom) subject was in a standing posture. The synchronized ECG signal (blue) indicates timing. (Hui et al., 2020.) 303

Figure 9.1 Comparison of 30-second records of AC coupled Doppler microwave radar sensed respiratory volume signal (top), reconstructed waveform (middle), and spirometer transducer output (bottom). 308

Figure 9.2 Computer X-ray tomographic (CT) images of the coronal section of the human chest: (a) CT of ambulatory subject with dry lungs (non-heart failure), and (b) CT of a patient showing pulmonary edema in congestive heart failure. 310

Figure 9.3 Magnetic resonance image of cerebral edema: (Left) Ventricular edema and (right) tumorigenic brain edema. 311

Figure 9.4 Changes in the baseline of the amplitude of the microwave reflection coefficient and left atrial pressure during development of pulmonary edema in an anesthetized 25 kg dog on a respirator. 313

Figure 9.5 Experimental results showing correlation between the phase of transmitted 915 MHz signal and the pulmonary arterial pressure in a dog during induction of pulmonary edema. (INF = infusion). 314

Figure 9.6 Radiometric response to injections of water in a model of the human thorax. The phantom model's emissivity decreases as the volume of water increases. 315

Figure 9.7 A functional block diagram of the wideband microwave automated scanning system. 315

Figure 9.8 Configuration of a coax-coplanar-waveguide-fed prototype slot antenna design: The evolution process of antenna 1 to antenna 5. 316

Figure 9.9 Differential scattering profile of lowest detectable fluid compared to normal cases with identical scaling: (a) 10 mL water, (b) normal; and (c) 4 mL water, (d) normal. (Rezaeieh et al., 2014.) 317

Figure 9.10 Details of wearable sensor antenna: active port 1 is the radio frequency transmitter and 15 passive ports serve as the receivers. (Courtesy of Asimina Kiourti, Ohio State University.) 318

Figure 9.11 Antenna placement on torso of mannequin and placement of porcine lungs inside the torso. (Courtesy of Asimina Kiourti, Ohio State University.) 318

Figure 9.12 Transmission coefficients of radio frequency signals measured using a prototype sensor system for diagnosis of pulmonary edema: (a) with porcine lung alone, (b) with six water balls inserted into the porcine lungs, and (c) with 12 water balls inserted into the porcine lungs. 319

Figure 9.13 Experimental arrangement of a near-field microwave pulmonary edema sensing system with an antenna array embedded inside a foam bed. (Rezaeieh et al., 2015.) 320

Figure 9.14 Images obtained using an 8 × 2 array configuration for a torso phantom: (Left) Normal artificial lungs without water and (right) abnormal artificial lungs with 1 mL inserted water. 321

Figure 9.15 Variation of the intensity of differential scattered field with the increase of water volume in the lungs using arrays of eight antennas (normalized with respect to the field value at 100 mL fluid volume).. 322

Figure 9.16 Images from using 8 × 2 antenna array configuration for a phantom torso with animal lungs: (Left) normal lamb lungs and (right) abnormal lamb lungs with 1 mL injected water. 322

Figure 9.17 A set of scattered field intensity images obtained from healthy volunteers. The high-intensity area corresponds to the location of the heart in the human volunteers. 323

Figure 9.18 A commercial noncontact near-field sensor with antennas embedded in a wearable vest over clothing. (Amir et al., 2016.) 324

Figure 9.19 Comparison of lung fluid level in participants (N = 31) quantitated using computerized tomography and noninvasive radio frequency sensing. 325

Figure 9.20 A noninvasive radio frequency pulmonary edema sensing system with an adhesive patch and a removable antenna sensor: (a) Sensor's front view and (b) adhesive patch. (Wheatley-Guy et al., 2020.) 326

Figure 9.21 Placement of the sensor and patch in the left anterior axillary. (Wheatley-Guy et al., 2020.) 326

Figure 9.22 Comparison of radio frequency-measured pulmonary fluid content based on subject's sitting versus supine body position............ 327

Figure 9.23 Correlation between computerized tomography and radio frequency-measured fluid contents in the lungs. 327

Figure 9.24 Experimental arrangement of the prototype system and test components, attachments, data collection, and signal flow of all sensors including commercial BIOPAC devices, chest belts, and a pneumotachometer (PTM) connected to a facemask. (Sharma et al., 2020.) 328

Figure 9.25 Correlation and agreement between near-field microwave sensors (NCS) and pneumotachometer (PTM) measured respiratory volume (RV) for all participants. The label shows a marker for each breathing mode, including conscious normal, deep, fast and breath-hold (BH), as well as spontaneous breathing in relaxation and attention states. Also shown are the scatter plot (top) with Pearson's correlation coefficient r, and Bland-Altman plot (bottom) showing bias m at the center (solid line), and the corresponding limits of agreement (dash lines) given by m ± 2.24 (σ). (Sharma et al., 2020.) 329

Figure 9.26 Microwave instrumentation for detection and monitoring of cerebral edema: 1) Microwave signal generator, 2) directional coupler, 3) antennas, 4) vector voltmeter, and 5) chart recorder. 331

Figure 9.27 Changes in the phase of microwave signal transmitted through the phantom head model. The ± signs associated with W and E correspond to addition or subtraction of 10 mL of water and ethanol. 332

Figure 9.28 Phase changes in microwave signal transmitted through a phantom head model in response to successive additions of a measured amount (in mL) of saline (mimicking cerebrospinal fluid [CSF]) 333

Figure 9.29 Schematic diagram of experimental setup for recording microwave phase change, electrocardiogram, and intracranial pressure. 334

Figure 9.30 Changes in relative phase, electrocardiogram (ECG), and intracranial pressure (ICP) following saline injections (see arrows) of 0.07 mL and 0.05 mL, respectively. 335

Figure 9.31 Relative phase and intracranial pressure (ICP) following suction (see arrow). A volume of 0.02 mL of saline was withdrawn into the syringe. 336

Figure 9.32 Maximum phase change versus maximum intracranial pressure (ICP) change for injection of aliquots. Volumes of aliquot are shown by symbols 336

Figure 9.33 Change in phase, electrocardiogram (ECG), and intracranial pressure (ICP) following a saline infusion (see upward arrow) of 0.16 mL/min. 337

Figure 9.34 Return of relative phase toward the baseline after cessation of a saline infusion (see downward arrow). 337

Figure 9.35 Transient changes in phase and intracranial pressure (ICP) associated with each heartbeat during a period of hypoxia. 338

Figure 10.1 Sleep stage, duration, and timeline cycled through during the night on a screen display. 347

Figure 10.2 A screen display showing 7-day sleep patterns compared to the prior 14-day average. ... 348
Figure 10.3 A wearable tracker as health monitor for vital signs such as respiration rate, heart rate, heart rate variability, and skin temperature. ... 349
Figure 10.4 Daily activity and comparison to "recovery" to normal weekly levels. ... 350
Figure 10.5 The standard three-lead configuration (I, II, and III) for electrocardiogram recording. ... 350
Figure 10.6 Normal single lead (lead I) electrocardiogram from a wrist-worn smartwatch sensor. ... 351
Figure 10.7 A modern Holter monitoring device for cardiac rhythm diagnosis. (From Medical Encyclopedia, Holter heart monitor, MedlinePlus [Internet]. Bethesda (MD): National Library of Medicine (US); [updated Jun 24; cited 2020 Jul 1]. Available from: https://medlineplus.gov/.) ... 352
Figure 10.8 Insulated electrodes for capacitive coupling sensors. ... 353
Figure 10.9 Schematic diagram of a miniature S-band microwave arterial pulse-wave sensor. The ribbon antenna is seen at the upper right corner within the transistor circle. ... 354
Figure 10.10 A wearable microwave sensor held in direct contact with the skin over the right temporal artery of the head using an elastic headband. ... 355
Figure 10.11 A wearable miniature S-band microwave sensor measuring superficial temporal artery pulse waves by direct contact through a thin dielectric with the scalp. ... 355
Figure 10.12 Positioning of the prototype microwave sensor and a subject's wrist. (McFerran et al., 2019.) ... 357
Figure 10.13 Measured radial artery results from a human subject's wrist using a voltage-controlled oscillator. ... 357
Figure 10.14 A wearable clip-on microwave sensor inside a plastic sleeve over clothing. ... 358
Figure 10.15 Microwave sensor board including integrated microwave circuit, patch antenna, filter, and microcontroller in transparent plastic clip-on badge holder. ... 359
Figure 10.16 Comparison between clip-on wearable microwave Doppler sensor (top) and commercial electrocardiogram monitor (bottom)-measured heart signals. ... 359
Figure 10.17 Clip-on wearable microwave sensor measurements taken from three different subjects. The top row of tracings was taken with horizontal polarization and the bottom row

corresponds to vertical polarization. The right-most data are for a subject with medically diagnosed Wolff-Parkinson-White syndrome. 360

Figure 10.18 Wearable microwave radar sensor with a self-injection locked oscillator (SILO) tag for monitoring the heartbeats of a person in motion. 361

Figure 10.19 The system architecture for a chest-worn self-injection locked oscillator (SILO) tag sensor for heart-rate monitoring. 361

Figure 10.20 A wearable self-injection locked oscillator (SILO) tag attached (see inset) to the subject's clothing. The FM receiver is located 30 cm away on a tripod along with a BIOPAC electrocardiogram monitor. (Courtesy of T.-S. Jason Horng, National Sun Yat-Sen University.) 362

Figure 10.21 Comparison of the Doppler microwave signal detected by the SILO tag (Upper trace in each panel) with the reference ECG signal (Lower trace) in a seated subject. The figure at top shows five characteristic points, A, B, C, D, and E, identifiable in a cycle of the Doppler waveform. Specifically, A - corresponds to the middle of the T-P interval, B - the peak of the P wave, C - the peak of the R wave, D - the beginning of the T wave, and E - the end of the T wave in the ECG 363

Figure 10.22 Comparison of the Doppler signal detected by the self-injection locked oscillator (SILO tag) (upper) with the reference electrocardiogram ECG signal (lower) in phase 2 of the experiment. 364

Figure 10.23 Computational simulation of 5.6 GHz electric-field distributions on virtual observation planes in front of the CSRR: (a) Simulation configuration for observations at distances of (b) 0.0, (c) 3.0, (d) 6.0, and (e) 10.0 mm. (Courtesy of Chao-Hsiung Tseng, National Taiwan University of Science and Technology.) 365

Figure 10.24 System block diagram of the ILO-CSRR or SO-CSRR sensor. (Courtesy of Chao-Hsiung Tseng, National Taiwan University of Science and Technology.) 366

Figure 10.25 Photograph of ILO-CSRR sensor: (a) Top view showing microcontroller unit (MCU) used to control the phase-lock-loop (PLL IC) and (b) the bottom view showing the finger/wrist pulse sensor location. (Courtesy of Chao-Hsiung Tseng, National Taiwan University of Science and Technology.) 366

Figure 10.26 Measurement setups for finger (a) and wrist (b) pulse sensing. (Courtesy of Chao-Hsiung Tseng, National Taiwan University of Science and Technology.) 367

Figure 10.27 Measured time-domain results of finger pulse detection using ILO-CSRR and photoplethysmography sensor (upper). 367

Figure 10.28 Examples of the measured time-varying wrist pulse wave detection using an ILO-CSRR sensor (lower) compared to photoplethysmography sensor (upper). 368

Figure 10.29 Model of an antenna and enclosure positioned on the skin over an artery with H for artery height and W for width. Note that the extent of expansion (height and width) of the artery is exaggerated for illustration. (Courtesy of Jessi Johnson, Blumio Inc.) 369

Figure 10.30 Photograph of mm-wave arterial sensor strapped on wrist of a subject for radial artery pulse measurement. (Courtesy of Jessi Johnson, Blumio Inc.) 369

Figure 10.31 Normalized radial artery waveform (Upper in each case) and frequency spectrum (Lower) obtained from a human subject with stronger signal (P1) and a subject with weaker signal (P2). 370

Figure 10.32 Wearable self-injection locked oscillator radar sensor positioned on a subject's chest for measurement of breathing activity. (Costanzo et al., 2023.) 371

Figure 10.33 Block diagram of wearable respiration monitor for breathing rate detection with radio frequency energy harvesting via system-on-a-chip. 371

Figure 10.34 Output voltage waveforms of the demodulator circuit: (a) normal breathing at 0.25 Hz (15 bpm) and (b) rapid breathing at 0.7 Hz (42 bpm). 372

Figure 10.35 Microwave TX and RX antennas connected to the software-defined radio (SDR) transceiver in a 3D-printed package. (Sharma et al., 2020.) 373

Figure 10.36 The laboratory setup to monitor heartbeat and respiration. (Sharma et al., 2020.) 374

Figure 10.37 Correlation and agreement between the near-field coherent sensing and electrocardiogram-measured heart rate for the entire dataset. The label shows a marker for each breathing mode, including conscious normal, deep, fast, and breath-hold (BH), as well as spontaneous breathing in relaxation and attention states. The scatter plot (top) with Pearson's correlation coefficient r and Bland-Altman plot (bottom) showing bias m at the center (solid line) and the corresponding limits of agreement (dashed line) given by m ± 1.96(σ). 374

Figure 10.38 Correlation (top) and limits of agreement (bottom) of the near-field coherent sensor compared to reference device for respiratory rate measurement (see also explanations in Figure 10.37)....... 375

Figure 11.1 A multisubject vital-sign sensing system combining self-injection-locked (SIL) radar with frequency-modulated continuous-wave (FMCW) and sum-difference pattern detection techniques. 381

Figure 11.2 Photograph of the experimental arrangement for detection of two test participants behind a wooden partition panel. (Courtesy of T.-S. Jason Horng, National Sun Yat-Sen University.)....... 382

Figure 11.3 Cumulative (1 s) frequency-modulated continuous-wave spectra for range (distance) detection. 382

Figure 11.4 Vital signs detected for participant 1: (a) Position fluctuations due to vital signs at participant position and (b) spectrum of position fluctuations corresponding to heartbeat and respiration. 383

Figure 11.5 Vital signs detected for participant 2: (a) Position fluctuations due to vital signs at participant position and (b) spectrum of position fluctuations corresponding to heartbeat and respiration. 383

Figure 11.6 Reconstructed image for positions of the two participants based on the range and azimuth information. (Courtesy of T.-S. Jason Horng, National Sun Yat-Sen University.)....... 384

Figure 11.7 Schematic diagram of a radar measurement system with four-channel network analyzer and a planar wide-beam array antenna and electrocardiogram (ECG) as a reference signal. 385

Figure 11.8 Normalized histograms of errors in estimating the heart rate using the directionally constrained minimization of power (DCMP) for one participant (black), DCMP for two participants (light black), and a single channel for two participants (dashed) compared to electrocardiogram measurements. 385

Figure 11.9 Dual-beam phased array radar detection scenario for two subjects using multiple-input, multiple-output (MIMO) beamforming techniques. (Courtesy of Mehrdad Nosrati, Stevens Institute of Technology.)....... 387

Figure 11.10 Photograph of assembled dual-beam CW radar system including the transmitting and receiving patch antenna arrays. (Courtesy of Mehrdad Nosrati, Stevens Institute of Technology.)....... 387

Figure 11.11 Measurement setup for the concurrent respiration monitoring of two participants using the dual-beam phased array CW radar sensor. (Courtesy of Mehrdad Nosrati, Stevens Institute of Technology.) 388

Figure 11.12 Frequency spectrum of two sets of detected signals for radar operating in single-beam mode and in dual-beam mode: (a) Mixed colliding signal for radar operating in the single-beam mode and (b) solid and dashed curves showing the output of beam #1 and #2, respectively under dual-beam mode. 389

Figure 11.13 Schematic diagram of a prototype monopulse CW Doppler radar system for concurrent respiratory monitoring of multiple subjects. 390

Figure 11.14 Experimental setup showing two participants inside a microwave anechoic chamber. (Islam et al., 2020.) 390

Figure 11.15 Radar sensor separated respiratory signatures (gray) and chest belt signals (black) for: (a) subject-1 and (b) subject-2, along with corresponding frequency spectra used to extract respiration rates for: (c) subject-1 and (d) subject-2. Measured breathing rates are 0.18 Hz for subject-1 and 0.35 Hz for subject-2, both values closely match the chest belt reference. 391

Figure 11.16 Schematic diagram of an integrated frequency-modulated continuous-wave (FMCW)-interferometry radar system. (Courtesy of Changzhi Li, Texas Tech University.) 393

Figure 11.17 Prototype sensor measured respiration and heartbeat signals of a participant: (a) Amplitude of I and Q channel output signals with detailed waveforms shown in insert and (b) normalized frequency spectrum after envelope detection. 394

Figure 11.18 Continuous spectrogram of radar-sensed heartbeat and respiration signals. (Courtesy of Changzhi Li, Texas Tech University.) 394

Figure 11.19 Differentiation of human targets from strong stationary clutter-return scenarios: (a) Range profile corresponding to detection of human subjects behind a glass wall with various stationary targets and human-signature-associated fluctuations and (b) extraction of a human target using standard deviation enhancements. 395

Figure 11.20 Integrated radar sensor to identify human subjects in a complex environment with multiple stationary clutters: (a) Experimental scene, (b) 2-D mapping result for the scenario, and (c) human subject isolation from the 2-D mapping experiment. (Courtesy of Changzhi Li, Texas Tech University.) 396

Figure 11.21 Photograph of the experimental scene with two participants in an indoor corridor for demonstrating integrated frequency-modulated continuous wave interferometry radar-enabled production of inverse synthetic aperture radar (ISAR) images. (Courtesy of Changzhi Li, Texas Tech University.) 397

Figure 11.22 A sequence of integrated frequency-modulated continuous wave interferometry radar-enabled inverse synthetic aperture radar (ISAR) images: (Frame 1) the ISAR image at the beginning of data acquisition, (Frame 2) the ISAR image at 7 seconds, (Frame 3) the ISAR image at 26 seconds, and (Frame 4) the ISAR image at 64 seconds. (Courtesy of Changzhi Li, Texas Tech University.) 398

Figure 11.23 Block diagram of K-band frequency-modulated continuous wave radar system with beamforming array. 399

Figure 11.24 Photograph of printed circuit board realization of K-band frequency-modulated continuous wave radar system with beamforming array: (a) Top view and (b) bottom view. (Courtesy of Changzhi Li, Texas Tech University.) 400

Figure 11.25 Experimental scene of short-range localization with a human subject and two objects (car and lamppost). (Courtesy of Changzhi Li, Texas Tech University.) 401

Figure 11.26 Result of the short-range localization experiment with a human subject and two stationary targets using a K-band radar sensor. (Courtesy of Changzhi Li, Texas Tech University.) 401

Figure 11.27 Human subject extraction with a standard deviation of 10 sequencing scans. (Courtesy of Changzhi Li, Texas Tech University.) 402

Figure 11.28 The modulation scheme for a frequency-shift keying radar system: (Top) Frequency-time representation and (bottom) amplitude-time representation for square-wave modulation. 402

Figure 11.29 Schematic diagram of a frequency-shift keying range-tracking radar system. (Courtesy of Changzhi Li, Texas Tech University.) 403

Figure 11.30 Photograph of range tracking using a 5.8 GHz frequency-shift keying radar for two participants walking simultaneously in opposite directions in an interior corridor. (Courtesy of Changzhi Li, Texas Tech University.) 403

Figure 11.31 Measurement data for two subjects walking in opposite directions in an interior corridor using a 5.8 GHz frequency-shift keying location-tracking radar. 404

Figure 11.32 Results measured for two subjects walking in the same direction in an outdoor open area using a 24 GHz frequency-shift keying location-tracking radar. 404

Figure 11.33 Software architecture of the parametric spectral estimation feature extraction algorithm: (Step I) data acquisition from the radar system; (Step II) feature extraction for range and phase information in parallel; and (Step III) detection and tracking vital signs...406

Figure 11.34 Experimental setup for vial-sign measurement of two seated subjects with frequency-modulated continuous wave (FMCW) Doppler radar: (a) Block diagram showing overview of subjects with reference sensor and (b) schematic diagram giving a top view of antenna and subject spacing. (Lee et al., 2019.) 407

Figure 11.35 Results from measurement of two subjects in the radar field: (a) Range estimation for subjects positioned at 130 and 300 cm from the radar, (b) real-time heart rate variation of the front subject at 130 cm, and (c) real-time heart rate for the back subject at 300 cm. (Lee et al., 2019.)................................408

Figure 11.36 Comparison of extracted peak values of the real-time heart-rate data of two subjects provided by radar and reference piezoelectric pulse sensor. 409

Figure 11.37 Measurement results for two targets: (a) Range estimation for two targets at 130 and 170 cm, respectively, (b) heart rate for the front subject at 130 cm, and (c) heart rate for the back subject at 170 cm. (Lee et al., 2019.) 409

Figure 11.38 Comparison between radar and reference sensor measured heart rates as functions of time... 410

Figure 11.39 Comparison between the algorithm-based radar and the reference sensor measured variations of heart rate for the subjects at front (Target1) and in back (Target2), (b) Frequency spectrum obtained by radar and reference sensor for the subjects in front (Target1) and back (Target2). 411

Figure 11.40 Measurement results of three participants located at 130, 180, and 300 cm away from the radar: (a) Range estimation, (b) comparison of heart rates between the radar method and the reference sensor as a function of time, and amplitude distribution of heart rates (beat/min): (c) for participant 1, (d) for participant 2, and (e) for participant 3. 412

Figure 11.41 Experimental results for two subjects at 100 and 140 cm: (a) Range estimation, (b) comparison of the respiration rate measured by frequency- modulated continuous wave

(FMCW) radar method with that of reference sensor, and (c) comparison of the heart rate of the proposed method with that of reference sensor. 415

Figure 11.42 Experimental scenario for two subjects lying side-by-side on a bed next to frequency-modulated continuous wave (FMCW) radar sensor. (Lee et al., 2020.) 416

Figure 11.43 Experimental results for two subjects lying side-by-side on a bed: (a) range estimation, (b) comparison of the respiratory rate (RR) obtained using the proposed radar method with commercial reference sensor, and (c) comparison of the HR obtained using the radar method with that by reference sensor.......... 417

Figure 11.44 The two participants at different ranges and separated side-by-side by 0.6 meters in between: (a) Experimental scenario and (b) 2-D-FFT range profile. (Dai, 2022; Courtesy of Vo Dai, Toan Khanh, University of Tennessee.) 419

Figure 11.45 Accuracy rate of heartbeat estimation for two participants (a and b). Horizontal axis shows: 1) Channel average with all channels, 2) Channel average with selected channels, 3) Channel with lowest RMS error, 4) MRC with all channels, and 5) MRC with selected channels. 419

Figure 11.46 TDM-phased multiple-input multiple-output sensor experimental setup for measurement of breathing and heartbeat signals of two participants. (Courtesy of Chung-Tse Michael Wu, Rutgers University.)................................ 421

Figure 11.47 Accuracy rate of two-subject measurement for different angles between two targets. The radar-to-target distance is 1.6 m: (a) Respiration and (b) heartbeat. 421

Figure 11.48 Experimental setup for participants not facing the radar sensor. (Courtesy of Chung-Tse Michael Wu, Rutgers University.) 422

Figure 11.49 Accuracy rate of two-subject measurement for different target orientations. The radar-to-target distance is 1.6 m and target angle of separation is 30°: (a) Respiration and (b) heartbeat.. 422

Figure 11.50 Sleep apnea–hypopnea syndrome (SAHS) monitoring system showing radar location under the patient bed. (Kagawa et al., 2016.).. 424

Figure 11.51 Functional block diagram of sleep apnea–hypopnea syndrome (SAHS) measurement system. 424

Figure 11.52 Respiratory signals from radar output: (a) Heartbeat superimposed on top of respiration; (b) hypopnea signal with amplitude <50% and apnea signal with amplitude <20%; (c) I/Q channel output signals; and (d) random body movement signal starting at 11 seconds. 425

Figure 11.53 Correlation of respiratory disturbance indexes between radar and PSG measurements. 425

Figure 11.54 Experimental setup for impulse-radio ultrawideband (IR-UWB) radar and polysomnography (PSG) measurement. IR-UWB radar on a bedside table is 1 meter above the floor and is less than 2 meters from the midline of a bed. (Kwon et al., 2022.) 427

Figure 11.55 Example of ultrawideband raw data and different normalized polysomnography (PSG) signals with normal breathing and three types of respiratory events: (a) normal without event, (b) central sleep apnea, (c) obstructive sleep apnea, and (d) hypopnea. The PSG signals were recorded at 500 Hz, and the UWB signals were sampled with 20 fps. 428

Figure 11.56 Scatter plots of estimated apnea-hypopnea index (AHI) using impulse-radio ultrawideband radar versus AHI obtained from the polysomnography reference for (a) total sleep time from all subjects and (b) Bland-Altman plot for visualization of the agreement between the AHIs for total sleep time. The gray line indicates equality in (a). The gray bold line and dark lines in (b) indicate the average difference (bias) and the average ±1.96 standard deviation, respectively. 429

Figure 11.57 Frequency-modulated continuous wave radar-detected patient breathing patterns with superimposed heartbeats during mechanical ventilation. 431

Figure 11.58 Frequency-modulated continuous wave radar monitored spontaneous breathing showing different breathing patterns. Each inspiratory cycle is characterized by a first peak (chest-wall expansion during inhalation), followed by a curved peak (during exhalation). 432

Figure 11.59 Smartphone application in an automated insulin delivery (AID) system. 435

Figure 11.60 The percentage of time children (a) and adults (b) in the two groups were in the target glucose range as measured by continuous glucose monitoring during week 22 and 23. Symbols represent hourly group median values, and shaded regions indicate the 25th and 75th percentiles. 436

Figure 11.61 The telehealth and telemedicine landscape: Access, barriers, modalities, and patient-provider benefits for successful implementation. 438

Figure 11.62 Bedside monitor display of electrocardiogram (ECG, pulse or heart rate, HR), photoplethysmography (PPG), oxygen saturation (SpO_2), breathing (respiratory rate, RR), and blood pressure for a patient during postsurgery recovery in an actual hospital environment. 439

Figure 11.63 Potential locations of radar vital-sign sensors inside a vehicle cabin. 440

Figure 11.64 Display of recovered vital-sign signals: (a) Estimated respiration signal, (b) autocorrelation function of the respiration signal, (c) estimated heartbeat signal, and (d) spectrum of heartbeat signal. 441

Figure 11.65 Example of a single-chip millimeter-wave radar estimated result versus reference for HR and RR. 441

Figure 11.66 Actual intensity (red) and depth (blue) obtained from NIR camera (a). Depth change induced by motion (blue rectangle) is inversely proportional to the intensity, which is a key source of errors in the HR reading. When motion clutters are present, they create noise frequency components that overwhelm the true HR signal (b). (From Guo et al., 2022.) 442

Table 1.1 Approximate Wavelength, Frequency, Common Uses, and Some Medical Applications of the Various Regions of the Electromagnetic Spectrum 5

Table 1.2 Internationally Designated Frequency Band of the RF and Microwave Regions of the Electromagnetic Spectrum 5

Table 1.3 Commonly Used Letter Band Designations of the Microwave Region of the Electromagnetic Spectrum 6

Table 1.4 Frequency and Wavelength in Air, Lungs, and Skin (Muscle) in the RF and Microwave Region of the Electromagnetic Spectrum 11

Table 3.1 Typical Radar Cross Section of Common Objects 84

Table 4.1 Permittivity of Common Low-Loss Dielectric Materials at 25°C 98

Table 4.2 Measured Temperature-Dependent Dielectric Permittivity of Animal Tissues at Microwave Frequencies 103

Table 4.3 Relative Permittivity (Dielectric Constant) and Conductivity of Tissues in the Human Head at 37°C 108

Table 5.1 Magnitude of Reflection Coefficient (in Percent) between Air and Tissue and between Biological Tissues at 37°C 123

Table 5.2 Depth of Penetration of Microwaves in Biological Tissues as a Function of Frequency 124

Table 5.3 Propagation Characteristics of Plane Waves in Low- and High-Water-Content Biological Tissues at 37°C 125

Table 6.1 Fourier Transform Pairs of Common and Specialized Functions 162

Table 7.1 Doppler Radar Compared to Conventional Respiration Belt Measurements Associated with Different Respiratory Disorders 190

Table 7.2 Accuracy of Radar Measurement for Various Motion Amplitudes 199

Table 7.3 Statistics of Microwave Sensor and Visual Determination of Heart and Respiration Rates of Adult Human Subjects (11 Readings for Each Parameter) 213

Table 8.1 Diagnostic Indications from Patients with Various Disease States According to Pulse-Wave Features 290

Table 8.2 Comparison of Intra-Aortic Catheter Pressure and Noninvasive Microwave Pulse-Wave Measurements for 5 Human Subjects 291

Table 8.3 Calibration Parameters of SBP-PTT and DBP-PTT for Human Subjects (S1, S2, and S3) 293

Table 8.4 Result of SBP/DBP Measurements Using Microwave Doppler Radar for 3 Human Subjects 293

Table 8.5 SILO Sensor-Measured Arterial Blood Pressures of 10 Subjects Aged 23 to 48 Years: BMI (Body Mass Index) 296

Table 8.6 Summary of Computed RMS Values of Radar and ECG-Measured HR for 12 Subjects 298

Table 9.1 Comparison of Dielectric Probe Measured, Estimated, and Sensor-Detected Values of Dielectric Permittivity from 2 Different Trials 320

Table 11.1 Performance Evaluation of Separated Respiration Signatures with Reference Respiration-Belt Reference Signals at Range Distances (1–3 m) for Two Different Angular Discriminations 391

Table 11.2 Representative Result of Heartbeat and Breathing Rate Estimations for Single-Target and Two-Target Scenarios 420

Table 11.3 Diagnostic Performance in the Test Group (35 Participants) 426

Table 11.4 SAHS Severity Classification and Diagnostic Performance 430

Table A.1 Standard prefixes used with units of the international system (SI) of measurements 449

Taylor & Francis
Taylor & Francis Group
http://taylorandfrancis.com

Preface

It has been known since the early 1970s that Doppler microwave radars can be applied to sense vital signs in humans and animals. The exponential growth of research and development in wireless microwave noninvasive sensing of physiological signatures and volume changes during the past two decades has prompted a special interest in this subject. As a result, there has been a massive outpouring of concepts, technology, and information aimed at achieving, quantifying, and applying connected technological advancements. However, in spite of the tremendous advancement in recent years, there are few textbooks that provide a broad, cohesive treatment in moderate depth of the essential elements of the various aspects of microwave radar sensing in physical fitness, sports medicine, and healthcare delivery. One objective of this book on noninvasive physiological measurement through wireless microwave sensing is to fulfill the need by presenting comprehensive and, amply illustrated coverage of the subject. It is intended for use as a textbook at the graduate or advanced undergraduate level, and as a source of general information for electronic engineers, biomedical scientists, and healthcare professionals interested in research and development of microwave noninvasive physiological sensing to help improve public and patient health.

The book begins with an introduction to the subject and sets off with a historical perspective on pioneering investigations in the subject area. To assist understanding of later materials and discussions, the next four chapters are structured to provide fundamental concepts and methods that underpin the specific themes of application that constitute the last five chapters of the book. Thus, Chapter 3 describes the principles and physical laws governing microwave propagation, reflection, and scattering to augment knowledge of microwave sensing. The two Chapters (i.e., Chapters 4 and 5) that follow are devoted to biophysical topics of the microwave property of biological materials and interactions with biological bodies, with an aim to facilitate an understanding of microwave physiological sensing. Chapter 6 discusses the principles of linear system analysis and signal processing alongside a brief overview of relevant software algorithms to augment detection and extraction of microwave physiological signals. Descriptions of specific algorithms involved in many of the investigations are included with the specific topics discussed in later chapters.

The plans for the rest of the book (i.e., Chapters 7–11) are to describe the leading applications alongside technical advantages and operating principles in each area. These chapters present in-depth discussions of vital-sign detection, monitoring of tissue-volume change and fluid redistribution, arterial pulse wave and pressure determination, wearable sensors, and contemporary applications and advanced topics in noninvasive microwave sensing and measurement. The guiding principles throughout are to start with brief introductions to the specific topics, relevant anatomical structure and physiology, supporting methodologies, and discussions on current state of knowledge, and then progress to incorporation of recent advances within the scope of each topical area. To facilitate an understanding of the measurements and differences in the various organ and tissue systems, essential anatomic and physiological background information is included, where appropriate. It is hoped that this approach will make it unnecessary to refer extensively to the basic textbooks. Nevertheless, specific and general references are given at the end of each chapter. These are provided for the convenience of the readers, who may wish to gain a more detailed knowledge of the subject under discussion, to put the materials in proper perspective, and to overcome potential misunderstanding. Furthermore, to help enhance the pedagogical significance and benefit, the basic and advanced topics described are accompanied by 354 figures and illustrations. I take this opportunity to acknowledge and express my thanks to the many authors for the privilege of reusing published figures, diagrams, or photos in whole or in part, as cited, for illustration in this book.

The many colleagues and students whose contributions to various aspects of the subjects covered in this book are recognized with appreciation. I would like to direct readers to the reference citations for their names that appear in our joint publications. I also wish to express my thanks to the many scientists and researchers for their invaluable suggestions and encouragements in composing the book. Indeed, their scientific works and technical innovations have been an inspiration in the preparation of this book. And importantly, it is with gratitude and love that the author thanks his family for their faith, support, and patience throughout the entire duration in writing this book.

James Chih-I Lin
University of Illinois Chicago

Acknowledgments

I would like to express my sincere thanks to those colleagues and fellow scientists and researchers for their magnanimous help in producing and providing various figures for illustration in the book. I am especially obliged to Huei-Ru Chuang, T. S. Jason Horng, Tzuen-Hsi Huang, Jessi Johnson, Asimina Kiourti, Changzhe Li, Lianming Li, Jenshan Lin, Mehrdad Nosrati, Eric Stewart, Toan Khanh Vo Dai, Chao-Hsiung Tseng, Fu-Kang Wang, and Chung-Tse Michael Wu in this regard.

About the Author

James C. Lin is Professor Emeritus at the University of Illinois, Chicago, where he has served as Head of the Bioengineering Department, Director of the Robotics and Automation Laboratory, and Director of Special Projects in Engineering. He held professorships in electrical and computer engineering, bioengineering, physiology and biophysics, and physical and rehabilitation medicine. He received BS, MS and PhD degrees in electrical engineering from the University of Washington, Seattle.

Dr. Lin is a Fellow of American Association for the Advancement of Science (AAAS), American Institute for Medical and Biological Engineering (AIMBE) and the International Scientific Radio Union (URSI), and a Life Fellow of the Institute of Electrical and Electronics Engineers (IEEE). He was recognized in Elsevier's top worldwide scientists in their fields for Career Impact and for Single-Year Impact in 2020. He held a National Science Council Research Chair from 1993 to 1997 and served for many years as an IEEE-Engineering in Medicine and Biology Society distinguished lecturer. He is a recipient of the d'Arsonval Medal from the Bioelectromagnetics Society, IEEE Electromagnetic Compatibility Transactions Prize Paper Award, IEEE COMAR Recognition Award, and CAPAMA Outstanding Leadership and Service Awards. He served as a member of U.S. President's Committee for National Medal of Science (1992 and 1993) and as Chairman of Chinese American Academic & Professional Convention (1993).

Professor Lin has served in leadership positions of several scientific and professional organizations including President of the Bioelectromagnetics Society, Chairman of URSI Commission on Electromagnetics in Biology and Medicine, Co-Chair of URSI Inter-Commission Working Group on Solar Power Satellite, Chairman of the IEEE Committee on Man and Radiation, Vice President US National Council on Radiation Protection and Measurements (NCRP), and member of International Commission on Nonionizing Radiation Protection (ICNIRP). He also served on numerous advisory committees and panels for the U.S. Congress, Office of the U.S. President, National Academy of Sciences, Engineering, and Medicine, National Research Council, National Science Foundation, National Institutes of Health, Marconi Foundation, and the World Health Organization.

He has authored or edited 15 books including the recent book on *Auditory Effects of Microwave Radiation* (Springer, 2021), authored 450 book chapters and journal and magazine articles, and made 300+ conference presentations. He has made many fundamental scientific contributions to electromagnetics in biology and medicine, including microwave auditory effects and microwave thermoacoustic tomography. He has pioneered several medical applications of radio frequency and microwave energies including invention of a minimally invasive microwave ablation treatment for cardiac arrhythmia, and the contact, contactless, and noninvasive microwave sensing of physiological signatures and vital signs. He has chaired several international conferences including IEEE, BEMS and ICST (founding chairman of Wireless Mobile Communication and Healthcare – MobiHealth Conference). He was Editor-in-Chief of the journal *Bioelectromagnetics* from 2006 to 2022, served as a magazine columnist, book series editor, guest editor, and member of the editorial boards of several journals. A member of Sigma Xi, Phi Tau Phi, Tau Beta Pi, and Golden Key honorary societies, and listed in *American Men and Women of Science*, *Who's Who in America*, *Who's Who in Engineering*, *Who's Who in the World*, and *Men of Achievement,* among others.

1 Introduction

Monitoring vital signs is an important clinical tool for healthcare practitioners since it can provide a wide range of diagnostic information about the patient with a relatively modest hardware setup. The standard clinical protocol for acquiring vital signs is to apply electrodes and sensors on the patient and wire them to a data acquisition unit, which is typically secured to the patient's body by a strap for continuous ambulatory recordings. For hospitalized patients, the bulky data acquisition unit is placed bedside with cables extending from the body, significantly compromising patient mobility, comfort, and tolerance. While these problems can be considered as inconveniences for adult patients that can be justified by the merits of continuous monitoring, the same experiences can pose as serious challenges for the pediatric population – not only is their physiology significantly different from that of adults, but the physical fragility of neonates and children demands that the vital-sign monitoring technologies intended for children should function as noninvasively as possible and be contactless and unobtrusive, where applicable.

Such technologies would have equally profound applications in monitoring patients with critical burns or victims of hazardous chemical or nuclear contamination. Furthermore, compared to adults, the bundle of cables connecting the electrodes, sensors, and acquisition units can exert excessive force on children's skin and body, restricting the natural movements in both inpatient and outpatient settings. Therefore, there is a great need for vital-sign monitors that are noninvasive, unobtrusive, and noncontact for direct coupling with a patient's body to enable continuous wireless recording and transmission of cardiopulmonary activities. It is desirable that the devices do not require the use of adhesives, gels, and abrasives for minimized impact on the skin, in general, and especially for neonate and children's skin [Ness et al., 2013]. Also, in the context of veterinary healthcare, animals present distinctive vital signs and have radically different skin coverings [Zhou et al., 2020]. Therefore, noninvasive, contactless, and unobtrusive vital-sign sensing would be advantageous. Furthermore, it could bring about a potential microwave radar-based application to differentiate human subjects from animal targets.

In recent years, there has been a dramatic increase in research on the use of microwave and radio frequency (RF) radars for noninvasive physiological measurements. In addition to vital signs, the investigations have involved contact, near-field, contactless, short-range, and remote detection and monitoring of physiological signals and signatures. The signals of interest are associated with physical and physiological movements as well as surface and volume changes in healthy organs and diseased tissues. This interest has been sparked, in part, by pioneering research showing electromagnetic energy, especially in the RF and microwave frequency range, that possesses reasonable dispersion and propagation loss with reliably accurate measurement from outside the body without puncturing or penetrating the skin. The rapid growth in semiconductor electronic fabrication, incredible development of the

DOI: 10.1201/9781003315223-1